Since January 2020 Elsevier has created a COVID-19 resource centre with free information in English and Mandarin on the novel coronavirus COVID-19. The COVID-19 resource centre is hosted on Elsevier Connect, the company's public news and information website.

Elsevier hereby grants permission to make all its COVID-19-related research that is available on the COVID-19 resource centre - including this research content - immediately available in PubMed Central and other publicly funded repositories, such as the WHO COVID database with rights for unrestricted research re-use and analyses in any form or by any means with acknowledgement of the original source. These permissions are granted for free by Elsevier for as long as the COVID-19 resource centre remains active.

Journal of Molecular Structure 1263 (2022) 133114

Contents lists available at ScienceDirect

Journal of Molecular Structure

journal homepage: www.elsevier.com/locate/molstr

Design, synthesis and characterization of novel Ni(II) and Cu(II) complexes as antivirus drug candidates against SARS-CoV-2 and HIV virus

Aprajita, Mukesh Choudhary*

Department of Chemistry, National Institute of Technology Patna, Patna, Bihar 800005, India

ARTICLE INFO

Article history:
Received 9 March 2022
Revised 6 April 2022
Accepted 16 April 2022
Available online 19 April 2022

Keywords:
Crystal structure
Hirshfeld Surface analysis
Powdered XRD analysis
SARS-CoV-2 virus
HIV-1 virus

ABSTRACT

This paper describes the structure-based design, synthesis and anti-virus effect of two new coordination complexes, a Ni(II) complex $[Ni(L)_2]$ (**1**) and a Cu(II) complex $[Cu(L)_2]$ (**2**) of (E)-N-phenyl-2-(thiophen-2-ylmethylene) hydrazine-1-carbothioamide(**HL**). The synthesized ligand was coordinated to metal ions through the bidentate-N, S donor atoms. The newly synthesized complexes were characterized by various spectroscopic and physiochemical methods, powdered XRD analysis and also X-ray crystallography study. Ni(II) complex $[Ni(L)_2]$(**1**) crystallize in orthorhombic crystal system with the space group *Pbca* with four molecules in the unit cell (a = 9.857(3) Å, b = 7.749(2) Å, c = 32.292(10) Å, $\alpha = 90°$, $\beta = 90°$, $\gamma = 90°$, Z= 4) and reveals a distorted square planar geometry. A Hirshfeld surface and 2D fingerprint plot has been explored in the crystal structure of Ni(II) complex $[Ni(L)_2]$ (**1**). Energy framework computational analysis has also been explored. DFT based calculations have been performed on the Schiff base and its metal complexes to study the structure-property relationship. Furthermore, the molecular docking studies of the ligand and its metal complexes with SARS-CoV-2 virus (PDB ID: 7BZ5) and HIV-1 virus (PDB ID: 6MQA) are also investigated. The molecular docking calculations of the Ni(II) complex $[Ni(L)_2]$ (**1**) and a Cu(II) complex $[Cu(L)_2]$ (**2**) with SARS-CoV-2 virus revealed that the binding affinities at inhibition binding site of receptor protein are 9.7 kcal/mol and -9.3 kcal/mol, respectively. The molecular docking results showed that the binding affinities of Ni(II) complex (**1**) and Cu(II) complex **(2)** against SARS-CoV-2 virus were found comparatively higher than the HIV-1 virus (-8.5 kcal/mol and -8.2 kcal/mol, respectively). As potential drug candidates, Swiss-ADME predictions analyses are also studied and the results are compared with Chloroquine (CQ) and Hydroxychloroquine (HCQ) as anti-SARS-CoV-2 drugs.

© 2022 Elsevier B.V. All rights reserved.

1. Introduction

Thiosemicarbazone Schiff base ligands are condensation products of thiosemicarbazide with suitable carbonyl compounds [1,2]. They have attracted enormous attention because of their significance in chemical and biological activities. Furthermore, their pharmacological applications are improved by the presence of heterocyclic moiety [3]. These compounds play an important role in coordination chemistry, coordinating to metal ions via azomethine nitrogen [4,5]. Copper and nickel complexes of heterocyclic thiosemicarbazone ligands are much interest to researcher in past several years. These having bidentate N, S binding sites have been extensively synthesised and characterised. Moreover, copper and nickel have the ability to form different co-ordination environment and geometries giving large scope in co-ordination chemistry [6]. The variable donating properties of co-ordinating sites of thiosemicarbazone Schiff base ligands produces complexes with structural diversities under different reaction conditions [7].

Recently, a series of copper and nickel complexes of thiosemicarbazones having heterocyclic moiety has been synthesised and found that the nature of heteroatomic ring attached to them can considerably influence the biological activities of these complexes [8–11]. These ligands and their complexes have been extensively studied exploring their biological properties, including antibacterial, antimalarial, antiviral, antioxidant, cytotoxic and antineoplastic [12–15]. Besides this, recently the world is in quest for effective drug to treat SARC-CoV-2. As virus effect is still on rise, there is an urgent need to develop effective drug to control the mortality rate which may rise in near future. A number of literatures are published exploring the anti-SARC-CoV-2 properties of Schiff base metal complexes [16–19]. This present work de-

* Corresponding author at: Chemistry, NIT Patna: National Institute of Technology Patna, National Institute of Technology Pa..., Ashok Rajpath, Patna, 800005, India.
E-mail addresses: aprajita.phd20.ch@nitp.ac.in (Aprajita), mukesh@nitp.ac.in (M. Choudhary).

https://doi.org/10.1016/j.molstruc.2022.133114
0022-2860/© 2022 Elsevier B.V. All rights reserved.

scribes the structure-based design, synthesis and anti-virus effect of two new coordination complexes, a Ni(II) complex [$Ni(L)_2$] (**1**) and a Cu(II) complex [$Cu(L)_2$] (**2**) of (E)-N-phenyl-2-(thiophen-2-ylmethylene) hydrazine-1-carbothioamide (**HL**) as antivirus drug candidates against SARS-CoV-2 and HIV virus. The molecular docking studies of the ligand and its metal complexes with SARS-CoV-2 virus (PDB ID: 7BZ5) and HIV-1 virus (PDB ID: 6MQA) are also investigated. The molecular docking calculations of the Ni(II) complex [$Ni(L)_2$] (**1**) and a Cu(II) complex [$Cu(L)_2$] (**2**) with SARS-CoV-2 virus revealed the binding affinity of -9.7 kcal/mol and -9.3 kcal/mol, respectively at inhibition binding site of receptor protein. The molecular docking results showed that the binding affinities of the Schiff base ligand (**HL**), Ni(II) complex [$Ni(L)_2$] **(1)** and Cu(II) complex [$Cu(L)_2$] **(2)** against SARS-CoV-2 virus were found comparatively higher than the HIV virus (-8.5 kcal/mol and -8.2 kcal/mol, respectively). In addition, the Ni(II) complex [$Ni(L)_2$] **(1)** was characterized by X-ray crystallography. A Hirshfeld surface and 2D fingerprint plot has been explored in the crystal structure of [$Ni(L)_2$] **(1)**. Quantum mechanical calculations were performed to investigate structure-property relationship. As potential drug candidates, Swiss-ADME predictions analyses are also studied and the results are compared with Chloroquine (CQ) and Hydroxychloroquine (HCQ) as anti-SARS-CoV-2 drugs. The present study suggests the therapeutic potential of the investigated Schiff base metal complexes as anti-virus drug candidates against SARS-CoV-2 and HIV virus.

2. Experimental

2.1. Methods and materials

2.1.1. Chemicals

All chemicals and the solvents used in this analysis were of analytical grade and used as procured. Thiophene-2-carbaldehyde, 4-phenylthiosemicarbazide, copper(II) acetate monohydrate, nickel(II) acetate tetrahydrate salt were obtained from Sigma-Aldrich and used without further purification.

2.2. Characterization techniques

Various physical and spectral methods (NMR, FT-IR and UV-Visible spectroscopy) were investigated for the characterization of the Schiff base ligand (HL) and its Ni(II) complex [$Ni(L)_2$] (**1**) and Cu(II) complex [$Cu(L)_2$] (**2**). Elemental analytical data and quantum mechanical calculations also applied for these purposes. The electronic spectra of the ligands and its complexes were taken on a Thermo scientific UV-Vis recording spectrophotometer Evolution-3000 in quartz cells. NMR spectra were recorded on a Bruker Advance HD 500 MHz FT-NMR Spectrometer. IR spectra were recorded in KBr medium on a Bruker-Alpha-Platinum-ATR spectrophotometer (500-4000 cm^{-1}). The C, H, and N determinations were made on an Elementar Vario EL III Carlo Erba 1108 analyzer.

2.3. Crystal structure determination

The single crystal X-ray diffraction data of the nickel(II) complex [$Ni(L)_2$] **(1)** collected at 296(2) K using Bruker SMART APEXII CCD diffractometer, equipped with graphite-crystal incident beam monochromator, and a fine focus sealed tube with Mo-Kα (λ= 1.54178 Å) and the X-ray source at the SAIF, IIT Madras, India. The Bruker SMART software and Bruker SAINT Software were used for data acquisition and data reduction, respectively. The structures were solved by direct methods and refined by full-matrix least-square calculations with the SHELXL-2018/3 software package [20]. All non-hydrogen atoms were refined anisotropically, and all hydrogen atoms on carbon were placed in calculated position, guided by difference maps and refined isotropically [21]. The molecular and crystal structures were plotted using ORTEP [22], PLATON, Mercury [23] and Diamond 3.2 k [24] programs.

2.4. Powdered X-ray diffraction study

Powder XRD patterns of the complexes are recorded on Brukar D8 advance spectro-photometer. X-ray diffractograms were recorded for the Schiff base ligand (**HL**) and its Cu(II) complex [$Cu(L)_2$] **(2)** with the help of X-ray diffractometer with Cu as anode material [25,26]. The pattern was recorded in the 2θ range of 0º to 80º with a potential difference of 40 kV and current 30mA using Cu-Kα radiation at λ = 0.15406 nm at a scan rate of 0.02º min^{-1}. Crystal size was estimated by Scherer's formula, $Cs = K\lambda/\beta 2\theta COS\theta$, k is constant (k= 0.94), λ is the wavelength used (λ=0.154 nm), $\beta 2\theta$ width at half maxima (FWHM) of the whole peaks by XRD patterns while θ is Bragg angle [27].

2.5. Hirshfeld surface analysis

The Hirshfeld surface is a useful graphical visualization tool used to analyze the nature of the intermolecular interactions in the crystal packing, quantified using the Crystal Explorer 17.5 software [28]. The Hirshfeld surface provides qualitative information about all intermolecular interactions at a time, whereas fingerprint plots produce the most efficient interactive graphics to obtain intermolecular interactions quantitatively inside the crystal packing. The molecular Hirshfeld surfaces (HSs) and their associated two-dimensional fingerprint plots (FPs) were generated for the Ni(II) complex [$Ni(L)_2$] **(1)** based on their crystallographic information file (cif), using *Crystal Explorer 17.5* software. The 3D graphical plots of the HSs are mapped over the d_{norm} (normalized contact distance) surface enables us to visualize the various intermolecular interactions in the crystal lattice and allows us to gain insight into the crystal packing behavior. The HS is reduced to 2D fingerprint plots by obtaining standard resolution of molecular HS on calculating the *d*i and *d*e for each surface point. The *d*i and *d*e are the distance to the Hirshfeld surface from the nearest internal nucleus (inside the Hirshfeld surface) and external nucleus (outside the Hirshfeld surface), respectively. Further, the data are binned into a discrete interval of *d*i and *d*e, to generate a 2D histogram with a scale of 0.2 Å. The 2D FPs give a summary of the frequency of each combination *d*i and *d*e across the surface of a molecule and indicates the interactions present as well as the relative area of the surface corresponding to those interactions [29,30]. The energy framework analysis is carried out in order to explore the intermolecular interaction energies between the molecular pairs within the cluster of radii 3.8 Å. These calculations were performed using *Crystal Explorer 17.5* combined with CE-B3LYP/6-31G(d,p) functional/basis set. The radius of the cylinder connected to the centroids of the pairs of molecules represents the magnitude of interaction energies and relative strength of the molecular packing in a different direction. Using energy framework analysis supramolecular architecture of the crystal structure can be visualized. [31–33].

2.6. Theoretical study

Theoretical calculations by density functional theory (DFT) were performed with regard to molecular structure optimization and HOMO-LUMO energies, etc. of Schiff base ligand (**HL**) and its Ni(II) complex [$Ni(L)_2$] (**1**) and Cu(II) complex [$Cu(L)_2$] (**2**). The geometry optimization of the ligands and complexes was performed at the ωB97X-D/6-311+G** level of theory in vacuum using the Gaussian16 software package [34] and cross-validated using the Spartan 16/18 parallel suite of programs [35] at the resources of the computational facility at Department of Chemistry, NIT Patna, India.

The dispersion-corrected DFT functional ωB97X-D [36] was chosen to accurately estimate the Vander walls interactions, which are expected to contribute greatly to the stability of the complexes. Global reactivity descriptors (units in eV), such as ionization potential (IP), electron affinity (EA), electro negativity (χ), chemical potential (μ), global hardness (η), global softness (σ) and global electrophilicity (ω), were calculated using the formula as based on Koopmans theorem.

2.7. Swiss-ADME analysis

Online computational approaches were made to predict absorption, distribution, metabolism, excretion (ADME) [37,38]. The computational prediction of drug could avoid the tremendous cost and time associated with the in vivo experiments, and has attracted more and more attention. A large variety of *in silico* methods share the objective of predicting ADMET parameters from molecular structure and their pharmacokinetic and physicochemical parameters [39]. For Schiff base ligand (**HL**) and its Ni(II) complex $[Ni(L)_2]$ (**1**) and Cu(II) complex $[Cu(L)_2]$ (**2**) were performed by ADME prediction analysis (http://www.swissadme.ch) [40].

2.8. Molecular docking study

The molecular docking studies were performed for Schiff base ligand (**HL**), Ni(II) complex $[Ni(L)_2]$ (**1**) and Cu(II) complex $[Cu(L)_2]$ (**2**) to analyze their binding affinity for selected virus proteins. The crystal structures of SARS-CoV-2 main protease was obtained from the Protein Data Bank [41] (PDB ID: 7BZ5; space group: *C121*; unit cell: a = 195.226Å, b = 86.417Å, c = 56.827Å, $\alpha = 90°$, $\beta = 100.19°$, $\gamma = 90°$) and used as receptor protein. Also, the X-ray crystallographic structure of the HIV-1 CA virus was retrieved from the protein data bank [42] (PDB ID: 6MQA; space group: *P6*; unit cell: a = 90.237Å, b = 90.237Å, c = 57.534Å, $\alpha = 90°$, $\beta = 90°$, $\gamma = 120°$) and used as receptor protein. Initially, the protein coordinates were refined by deleting all the water and heteroatoms to make the targeted protein receptor-free. Further, the polar hydrogens and Kollman charges were added to the protein using the *Autodock tool* (ADT) 1.5.6 associated with *Autodock 4.2* software [43]. The prepared protein and ligand coordinates are saved in a pdbqt file format using ADT software. The gird box of the desired volume is selected in such a way that the ligand can rotate freely inside the active site pocket protein. The configuration files are generated using the coordinates and dimension of the grid box. *Vina Lamarckian* genetic algorithm [44] generates the output files having predicted free energy for binding sites. The result comprises of different poses with corresponding energies were analyzed and high-quality figures are rendered by open-source Discovery Studio visualizer [45].

2.9. General procedure for synthesis

2.9.1. Synthesis of (E)-N-phenyl-2-(thiophen-2-ylmethylene) hydrazine-1-carbothioamide (HL)

To synthesize the targeted thiosemicarbazone Schiff base ligand (**HL**), 4-phenylthiosemicarbazide (2.0 mmol, 0.334g) was taken in ethanol (10 mL) with dropwise addition of ethanolic solution of thiphene-2-carbaldehyde (2 mmol, 0.27mL). The stirred mixture was refluxed for 2-3 h. Off-white colour shiny crude product was obtained. Anal. Calcd for $C_{12}H_{11}N_3S_2$ **(HL):** C, 55.15%; H, 4.24%; N, 16.08%. Found: C, 55.08%; H, 4.22%; N, 16.07%.; FAB-mass (m/z): Obs. (Calcd.) 261.04 (261.37 g/mol.); ^{1}H-NMR (500 MHz, DMSO-d_6): δ 8.34 (*s*, 1H, -N=CH), δ 7.55 (*s*, 1H, Ar-H), δ 7.19 (*s*, 1H, Ar-H), δ 9.81 ppm (H, -N-H), δ 11.82 ppm (H, -N-H) (Figure S1). ^{13}C-NMR (500MHz, DMSO-d6): δ 176.04, 139.45, 138.85, 138.54, 131.40, 129.71, 128.57, 125.45, 125.83, 125.69 and 40.03 ppm (Figure S2). IR data (KBr/cm^{-1}): 1589 (>C=N); 782 (υC=S), 3292(υ N-H) (Figure S3). UV-Vis (DMSO) λ (nm): 367(π-π^*) and 328 (n-π^*) (Figure S6).

2.9.2. Synthesis of bis{N-phenyl-N'-[(thiophen-2-yl) methylidene] carbamohydrazonothioato}-nickel(II), $[Ni(L)_2]$ (1)

To a solution of **HL** (1 mmol, 0.261g) in acetonitrile (10 mL), triethylamine (1.0 mmol, 0.680 mL) is added dropwise. The mixture was stirred for half an hour. This mixture was then added dropwise to the methanolic solution of nickel(II) acetate tetrahydrate salt (0.5 mmol, 0.124g). The resultant solution was stirred for 4-5 hrs. After completion of reaction, the reaction mixture was filtered and was left for slow evaporation at room temperature. Brown colour crystals suitable for single crystal XRD for Ni(II) complex $[Ni(L)_2]$ (**1**) was obtained after a week. Anal. Calcd for $C_{24}H_{20}N_6NiS_4$ **(1)** (579.40g/mol) C, 49.75%; H, 3.48%; N, 14.51%. Found: C, 49.76%; H, 3.49%; N, 14.52%. FAB-mass (m/z): Obs. (Calcd.) 579.40 (579.43 g/mol.); IR data (KBr/cm^{-1}): 1586 (>C=N), 743 (υC=S), 536 (υNi-S), 582 (υNi-N), 3373 (υ N-H) (Figure S4). UV-Vis (DMSO) λ (nm): 372 (π-π^*) and 295 (n-π^*) (Figure S6).

2.9.3. Synthesis of bis{N-phenyl-N'-[(thiophen-2-yl)methylidene] carbamohydrazonothioato}-copper(II), $[Cu(L)_2]$ (2)

The Cu(II) complex $[Cu(L)_2]$ (**2**) was synthesized in a similar fashion as Ni(II) complex $[Ni(L)_2]$ (**1**) by adding copper(II) acetate monohydrate salt (0.5 mmol, 0.100g) instead of nickel(II) acetate tetrahydrate salt. The resultant solution was stirred for 4-5 hrs. After completion of reaction, the reaction mixture was filtered and was left for slow evaporation at room temperature. Green colour weak crystals were obtained. Anal. Calcd. for $C_{24}H_{20}CuN_6S_4$ (**2**) (584.25 g/mol) C, 49.34%; H, 3.45%; N, 14.38%. Found: C, 49.31%; H, 3.44%; N, 14.36%. FAB-mass (m/z): Obs. (Calcd.) 584.25 (584.27 g/mol.); IR data (KBr/cm^{-1}): 1587 (>C=N), 744 (υC=S), 539 (υNi-S), 582 (υNi-N), 3373 (υ N-H) (Figure S5). UV-Vis (DMSO) λ (nm): 371(π-π^*) and 310 (n-π^*) (Figure S6).

3. Results and discussion

3.1. Synthesis and characterization

This paper describes the structure-based design, synthesis and anti-virus effect of two new coordination complexes, a Ni(II) complex $[Ni(L)_2]$ (**1**) and a Cu(II) complex $[Cu(L)_2]$ (**2**) of (E)-N-phenyl-2-(thiophen-2-ylmethylene) hydrazine-1-carbothioamide(**HL**). A protocol used for the synthesis of the Schiff base ligand **HL** and its Ni(II) complex $[Ni(L)_2]$ (**1**) and Cu(II) complex $[Cu(L)_2]$ **(2)** is presented in the Scheme 1. The synthesized ligand was coordinated to metal ions through the bidentate-N, S donor atoms. The newly synthesized complexes were characterized by various spectroscopic and physiochemical methods, powdered XRD analysis and also X-ray crystallography study. Complex $[Ni(L)_2]$ **(1)** crystallized in the orthorhombic crystal system with the space group *Pbca* with four molecules in the unit cell (a = 9.857(3) Å, b = 7.749(2) Å, c = 32.292(10) Å, $\alpha = 90°$, $\beta = 90°$, $\gamma = 90°$, Z= 4) and reveals a distorted square planar geometry. A Hirshfeld surface and 2D fingerprint plot has been explored in the crystal structure of complex **(1)**. DFT based calculations have been performed on the Schiff base and its metal complexes to study the structure-property relationship. Furthermore, the molecular docking studies of the ligand and its metal complexes with SARS-CoV-2 virus (PDB ID: 7BZ5) and HIV-1 virus (PDB ID: 6MQA) are also investigated. The molecular docking calculations of the complex (**1**) and (**2**) with SARS-CoV-2 virus revealed that the binding affinities at inhibition binding site of receptor protein are 9.7 kcal/mol and -9.3 kcal/mol, respectively. The molecular docking results showed that the binding affinities of Ni(II) complex $[Ni(L)_2]$ (**1**) and Cu(II) complex $[Cu(L)_2]$ **(2)** against

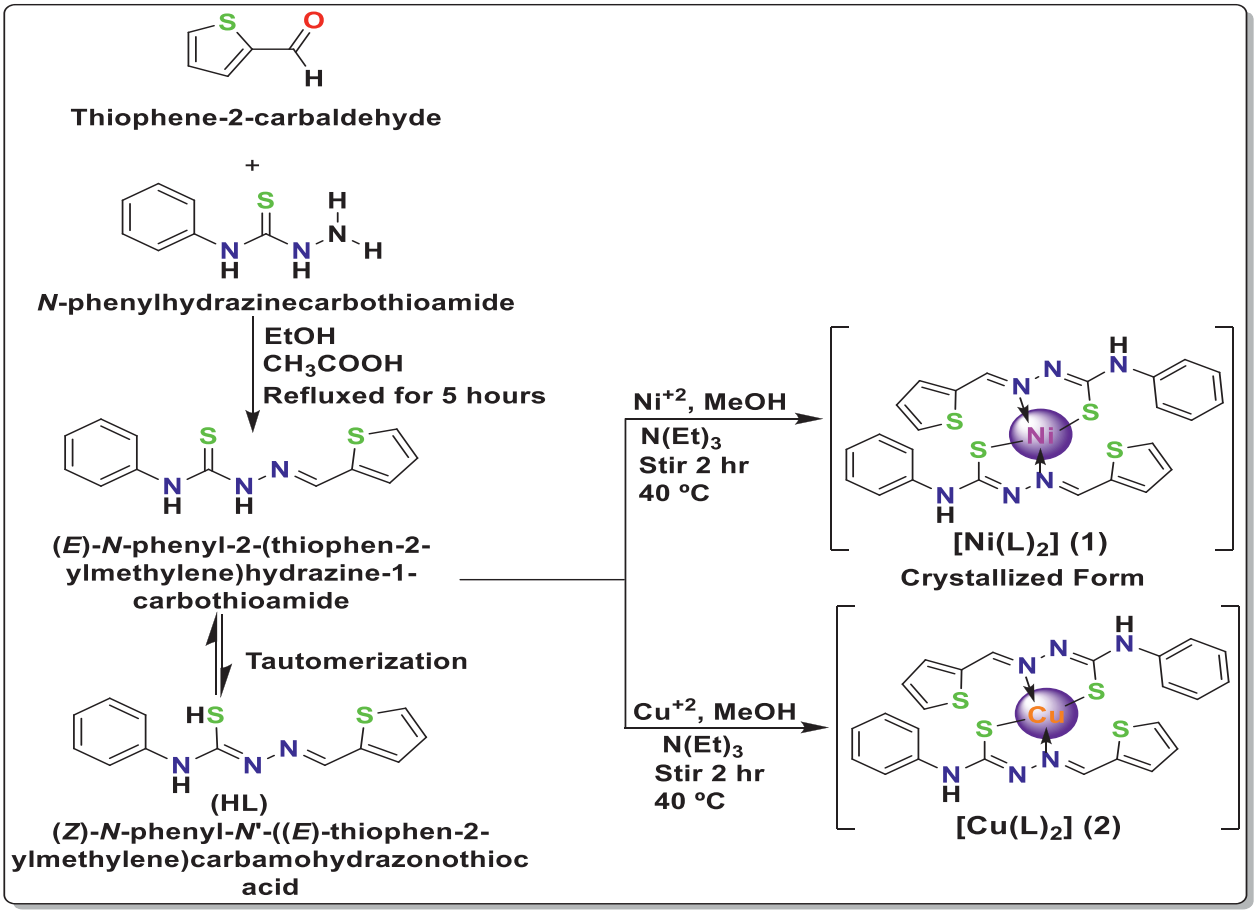

Scheme 1. Synthetic routes for the thiosemicarbazone Schiff base ligand (**HL**) and its Ni(II) complex [Ni(L)$_2$] (**1**) and Cu(II) complex [Cu(L)$_2$] (**2**).

SARS-CoV-2 virus were found comparatively higher than the HIV-1 virus (-8.5 kcal/mol and -8.2 kcal/mol, respectively). As potential drug candidates, Swiss-ADME predictions analyses are also studied and the results are compared with Chloroquine (CQ) and Hydroxychloroquine (HCQ) as anti-SARS-CoV-2 drugs. The present study suggests the therapeutic potential of the investigated Schiff base metal complexes as anti-virus drug candidates against SARS-CoV-2 and HIV virus.

3.2. Crystallographic description of [Ni(L)$_2$] (1)

The ORTEP structure of nickel(II) complex [Ni(L)$_2$] **(1)** along with atom labeling scheme is shown in Fig. 1, crystallographic data are tabulated in Table 1 and selected bond length and bond angle are tabulated in Table 2. Single-crystal X-ray diffraction reveals that Ni(II) center exhibits a distorted square planar geometry coordinated [46] to two symmetrically equivalent thiosemicarbazone Schiff base anions which completely balances Ni^{+2} cation. Each of the ligand is attached to the nickel center through azomethine nitrogen (N3, $N3^i$) and thiolate sulfur (S1, $S1^i$) atom of the deprotonated form after thiol formation [47].The bis-chelated nickel(II) complex [Ni(L)$_2$] **(1)** lie on a crystallographic inversion center and coordinate to the N and S atoms of the **HL** ligand to form two five-membered chelating rings (Ni1-S1-C7-N2-N3 and $Ni1\text{-}S1^i\text{-}C7^i\text{-}N2^i\text{-}N3^i$). The Ni1-N3 and $Ni1\text{-}N3^i$ are same which is equal to 1.9020(14) Å, while the Ni-S1 and $Ni\text{-}S1^i$ are also same which is equal to 2.1790(6) Å. The environment around Ni(II) ion in this complex is distorted square planar [48] which is evident from the cis angles N3-Ni1-S1(85.27(4)°), $N3^i\text{-}Ni1\text{-}S1^i$(85.27(4)°), $N3^i$-Ni1- S1(94.73(4)°) and N3-Ni1- $S1^i$(94.73(4)°), which deviates from 90°. The both the trans angels [49] $S1\text{-}Ni1\text{-}S1^i$ and $N1\text{-}Ni1\text{-}N1^i$ are equal to 180°. The bond length of azomethine C=N function is equal to 1.298 which is very close to the values reported in the literature for similar compounds. Careful examination of crystal packing in [Ni(L)$_2$] **(1)** reveals the presence of significant hydrogen bonds (Fig. 2 & S7, Table 3). This complex consists of an intermolecular C-H….S and C-H….N non classical hydrogen bond interactions C(2)-H(2)...N(2),C(2)-H(2)...S(2),C(8)-H(8)...S(1)#1, C(10)-H(10)...S(1)#2 with D…A distance equal to 2.916(2) Å, 3.481(2) Å, 3.1220(17) Å and 3.7719(19) Å, respectively [50].

3.3. Powdered XRD studies

The XRD study (powder pattern) of the Schiff base ligand (HL) and its copper complex (**2**) was made with the help of X-ray diffractometer with Cu as anode material, Kα [Å] = 0.15406 nm and the generator settings 30 mA, 40 kV. Powdered XRD patterns of the **HL** and its copper (II) complex [Cu(L)$_2$] (**2**) is presented in Fig. 3 which is recorded in the range of 2θ = 0-80º. Several diffraction peaks are observed which confirm the polycrystalline step in the pattern. The XRD pattern is indicative of their crystalline in nature which is confirmed by the main peaks positioned. The XRD patterns of the Schiff base was observed at 2θ = 22.36º for **HL,** which is characteristic peak for a Schiff base imine [51]. The XRD patterns clearly prove for the formation of copper (II) complex [Cu(L)$_2$] (**2**), since the crystalline index of Schiff base ligand **HL** at 2θ = 22.36º shifted to 2θ = 12.84 ºdue to π-π conjugation between the ligand and metal which confirms the existence of Cu ion in the ligand environment [52]. The average crystalline size (D)

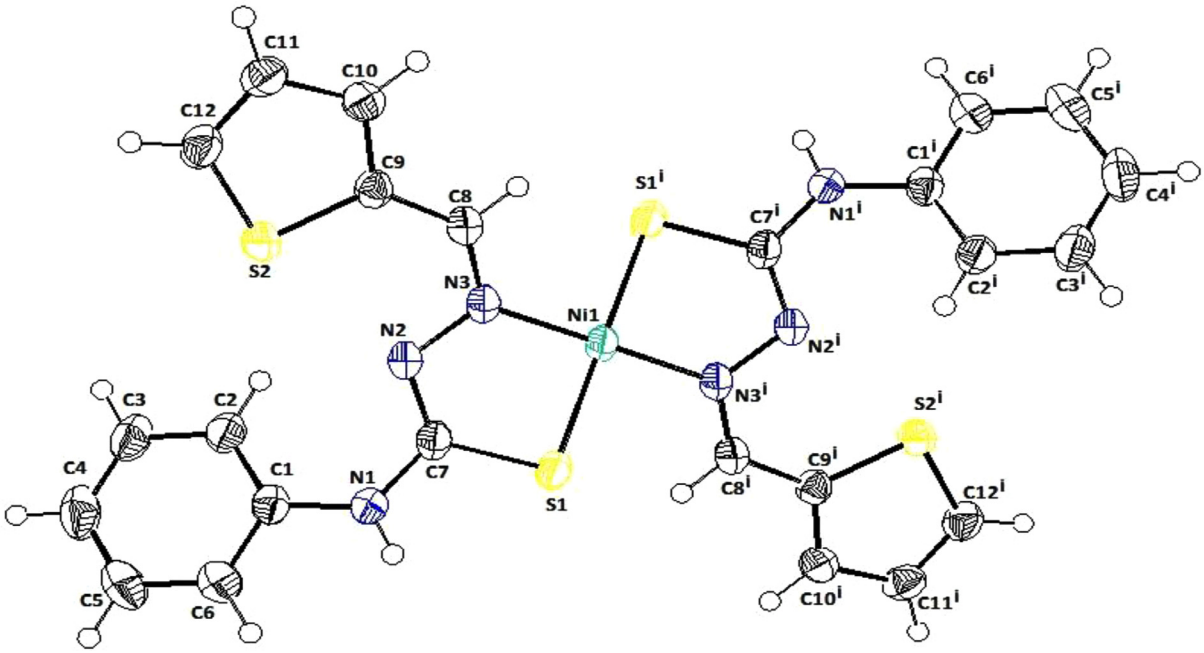

Fig. 1. ORTEP diagram of nickel complex [Ni(L_2)] **(1)** with 50% thermal ellipsoid and with atom numbering scheme.

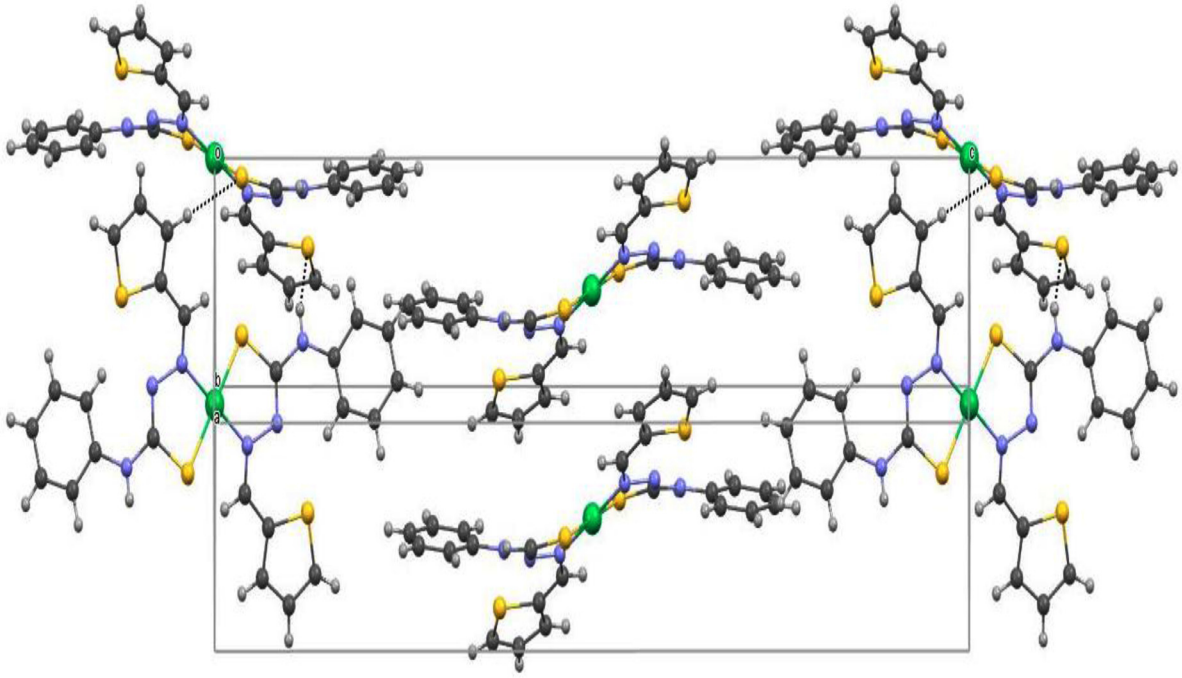

Fig. 2. View of crystal packing for Ni(II) complex [Ni(L_2)] **(1).**

of the Cu(II) complex [Cu($L)_2$] (**2**) was calculated using Scherer's formula and is found to be 55.52 nm [27].

3.4. FT-IR and UV-Vis spectroscopy

FT-IR spectra of Schiff base (**HL**) and its Ni(II) complex [Ni($L)_2$] (**1**) and Cu(II) complex [Cu($L)_2$] (**2**) are presented in Figure S3, S4 and S5, respectively. The IR spectrum exhibited an absorption peak at 1589 which can be assigned to azomethine group (HC=N). This peak is also present in IR spectrum of complexes but has shifted to lower frequency (1586 (>C=N) for [Ni($L)_2$] **(1)**; 1587 (>C=N) for [Cu($L)_2$] **(2)**, due to electronic delocalization after complex formation. IR spectroscopic data of both the metal complexes shows that the Schiff base ligand (**HL**) coordinate to metal ion through azomethine nitrogen and thiolate sulfur atom [536 (υNi-S), 582 (υNi-N) for [Ni($L)_2$] **(1)**; 539 (υNi-S), 582 (υNi-N) for [Cu($L)_2$] **(2)]** of the deprotonated form after thiol formation [53]. The electronic absorption spectra of **HL**, Ni(II) complex [Ni($L)_2$] (**1**) and Cu(II) complex [Cu($L)_2$] (**2**) were recorded in DMSO solvent at RT (Figure S6). The electronic transitions observed in ligand due to imine function of thio-semicarbazone moiety were slightly shifted on complexation with metal. UV-Vis spectra [1] of **HL** show two bands, first at 328 nm corresponding to n→π^* transition in the thiosemicarbazone group, and second one at 367 nm corresponding to $\pi \rightarrow \pi^*$

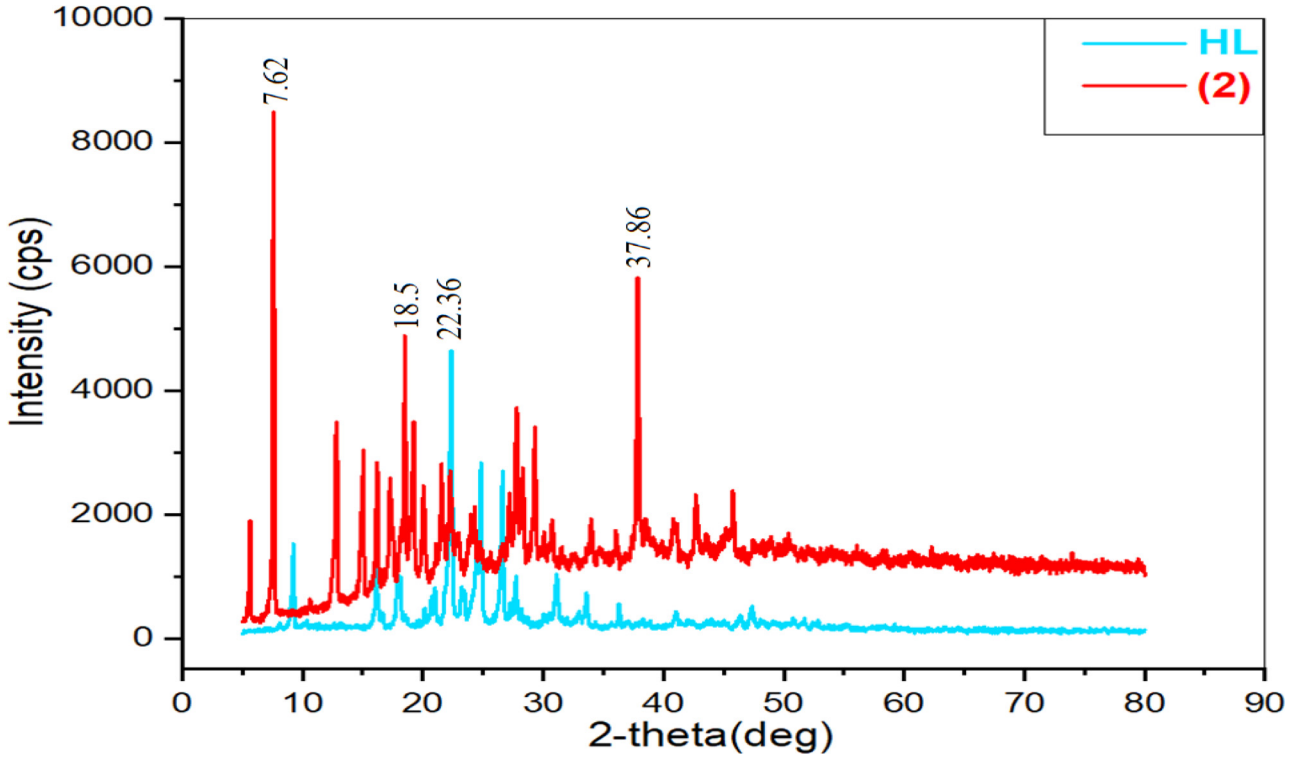

Fig. 3. Powdered XRD pattern of thiosemicarbazone Schiff base ligand (**HL**) and its Cu(II) complex [$Cu(L_2)$] **(2)**.

Table 1
Crystallographic Data and Refinement Parameters for Ni(II) complex [$Ni(L_2)$] **(1)**.

Crystallographic data	**(1)**
Formula	$C_{24}H_{20}N_6NiS_4$
Mw ($gmol^{-1}$)	579.41
temp (K)	180(2)
λ (Mo Kα), (Å)	0.71073
crystal system	Orthorhombic
space group	Pbca
a (Å)	9.857(3)
b (Å)	7.749(2)
c (Å)	32.292(10)
α (°)	90
β (°)	90
γ (°)	90
V ($Å^3$)	2466.5(12)
Z	4
D_{calc} (Mg/m^3)	1.560
μ (mm^{-1})	1.152
F(000)	1192
Crystal size(mm^3)	0.190 × 0.170 × 0.050
Index ranges	-13<=h<=13, -10<=k<=10, -44<=l<=44
Collected reflections	75067
unique reflections	3488 [R(int) = 0.0811]
Absorption correction	Semi-empirical from equivalents
max and min trans	0.679 and 0.562
Refinement method	Full-matrix least-squares on F^2
Data / restraints / parameters	3488 / 0 / 163
Goodness-of-fit (GOF) on F^2	1.070
R1 [$I > 2\sigma(I)$][a]	0.0316 & 0.0769
wR2 (all data)[b]	0.0384 & 0.0817
CCDC Number	2152930

[a] $R_1 = \Sigma \| |F_o| - |F_c| | / \Sigma |F_o|$.
[b] $wR_2 = \{\Sigma [w(F_o^2 - F_c^2)^2] / \Sigma [w(F_o^2)^2]\}^{1/2}$.

Table 2
Bond distances (Å) and bond angles (°) for Ni(II) complex [$Ni(L_2)$] **(1)**.

Bond lengths (Å)			
Ni(1)-S(1)#1	2.1790(6)	C(7)-S(1)	1.7383(16)
C(8)-N(3)	1.298(2)	C(9)-S(2)	1.7281(17)
N(2)-N(3)	1.3980(18)	Ni(1)-N(3)#1	1.9020(14)
Ni(1)-N(3)	1.9020(14)	Ni(1)-S(1)	2.1790(6)
Bond angles (°)			
N(3)#1-Ni(1)-N(3)	180.0	S(1)-Ni(1)-S(1)#1	180.00(2)
N(3)#1-Ni(1)-S(1)	94.73(4)	N(3)-Ni(1)-S(1)#1	94.73(4)
N(3)#1-Ni(1)-S(1)#1	85.27(4)	N(3)-Ni(1)-S(1)	85.27(4)
C(8)-N(3)-Ni(1)	125.87(11)	N(2)-N(3)-Ni(1)	119.70(11)

Table 3
Hydrogen bonds for Ni(II) complex [$Ni(L_2)$] **(1)**.

D-H...A	d(D-H)	d(H...A)	d(D...A)	<(DHA)
C(2)-H(2)...N(2)	0.95	2.33	2.916(2)	119.6
C(2)-H(2)...S(2)	0.95	2.86	3.481(2)	123.8
C(8)-H(8)...S(1)#1	0.95	2.56	3.1220(17)	118.2
	0.95	2.92	3.7719(19)	149.2
C(10)-H(10)...S(1)#2	0.82(2)	3.04(2)	3.5409(19)	122.0(18)
N(1)-H(1N)...S(2)#3				

Symmetry transformations used to generate equivalent atoms: #1 -x,-y,-z #2 x-1/2,-y+1/2,-z #3 -x+1/2,y-1/2,z.

of the phenyl ring; while Ni(II) complex [$Ni(L)_2$] (**1**) shows peak at 295 for n→π* and at 372 for π→π*; similarly, Cu(II) complex [$Cu(L)_2$] (**2**) shows peak at 310 for n→π* and at 371 for π→π*. The shift of the bands due to intra ligand transitions is the result of weaking of the C=S bond and the extension of conjugation upon complexation. The shift occurs also due to coordination through sulphur of thiosemicarbazone group and azomethine nitrogen and

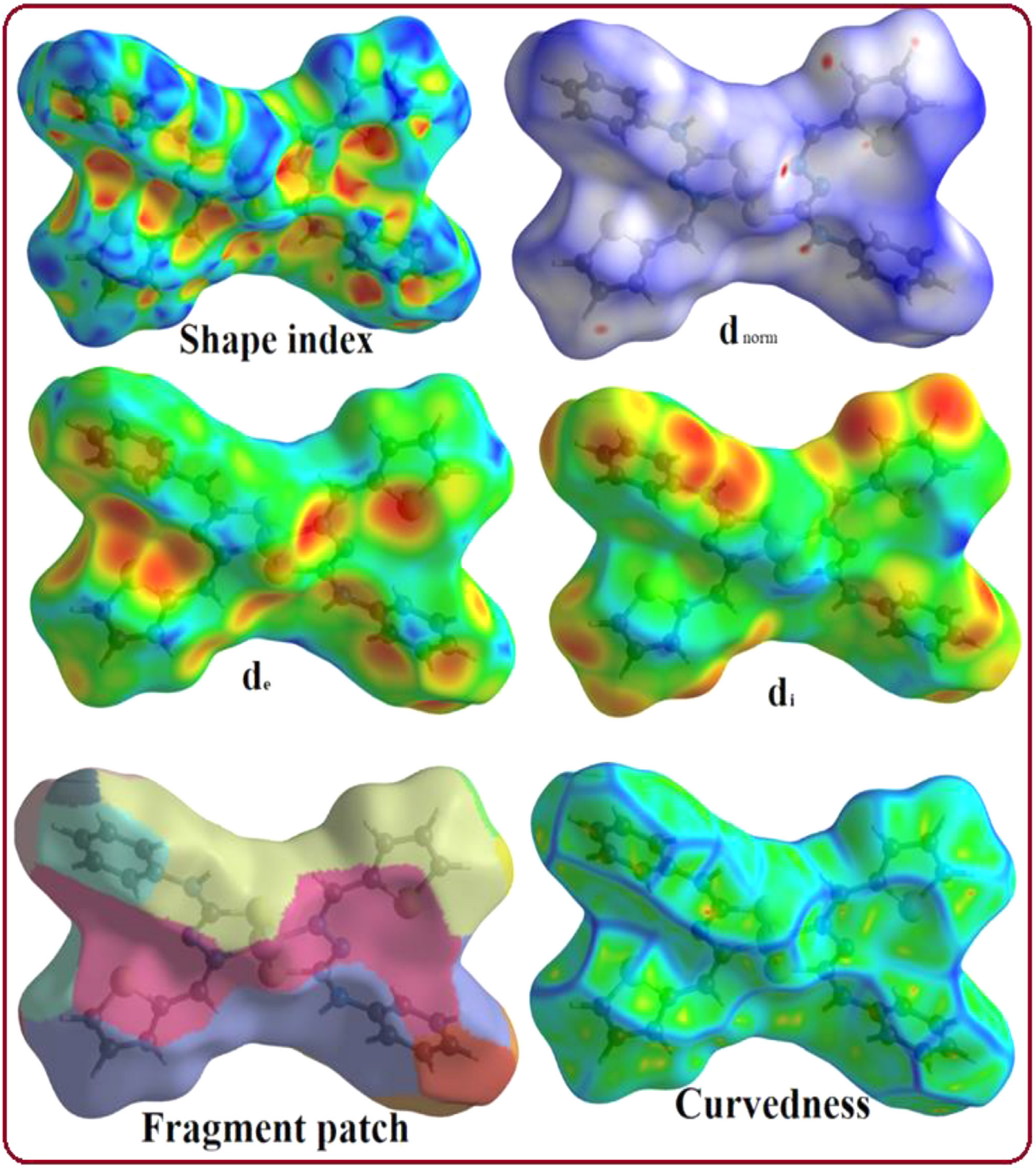

Fig. 4. Graphical view of the Hirshfeld surfaces mapped with d_{norm} property visualizing the interaction of the Ni(II) complex [Ni(L_2)] **(1)**: d_{norm} color scale in between -0.59 au (blue) and 2.07au (red). Shape index surfaces: (Red Color-Hollows, bumps-blue colors). Curvedness: (edges-blue color; flat region-green color).

is indication of thio-enolization followed by deportation of the ligand during complexation. The broadness (Figure S4) of these bands can be explained as due to the combination of N→Cu/Ni, S→Cu/Ni LMCT transitions [6].

3.5. Hirshfeld surface analysis

The Hirshfeld surface [54] (HS) for nickel(II) complex [Ni($L)_2$] **(1)** is analyzed to evaluate the intermolecular interaction in the crystal system. Hirshfeld shape index, d_{norm}, d_e, d_i, fragment patch and curvedness surfaces of [Ni($L)_2$] **(1)** was presented in Figs. 4 and 2D-fingerprint plot showing all characteristics features of their short interaction was presented in Fig. 5. The globularity of [Ni($L)_2$] **(1)** is found to be 0.653, which supports that the molecular structure is more structured and not a sphere [46]. The asphericity of the crystal is found to be 0.286 which is measure of anisotropy. The d_{norm} HS was mapped over the range of -0.0542(red) to 1.3015(blue), where the red and white color indicate the strongest and intermediate interactions, respectively. Negligible intermolecular interaction is indicated by blue color. C-H…S and C-H…N non-

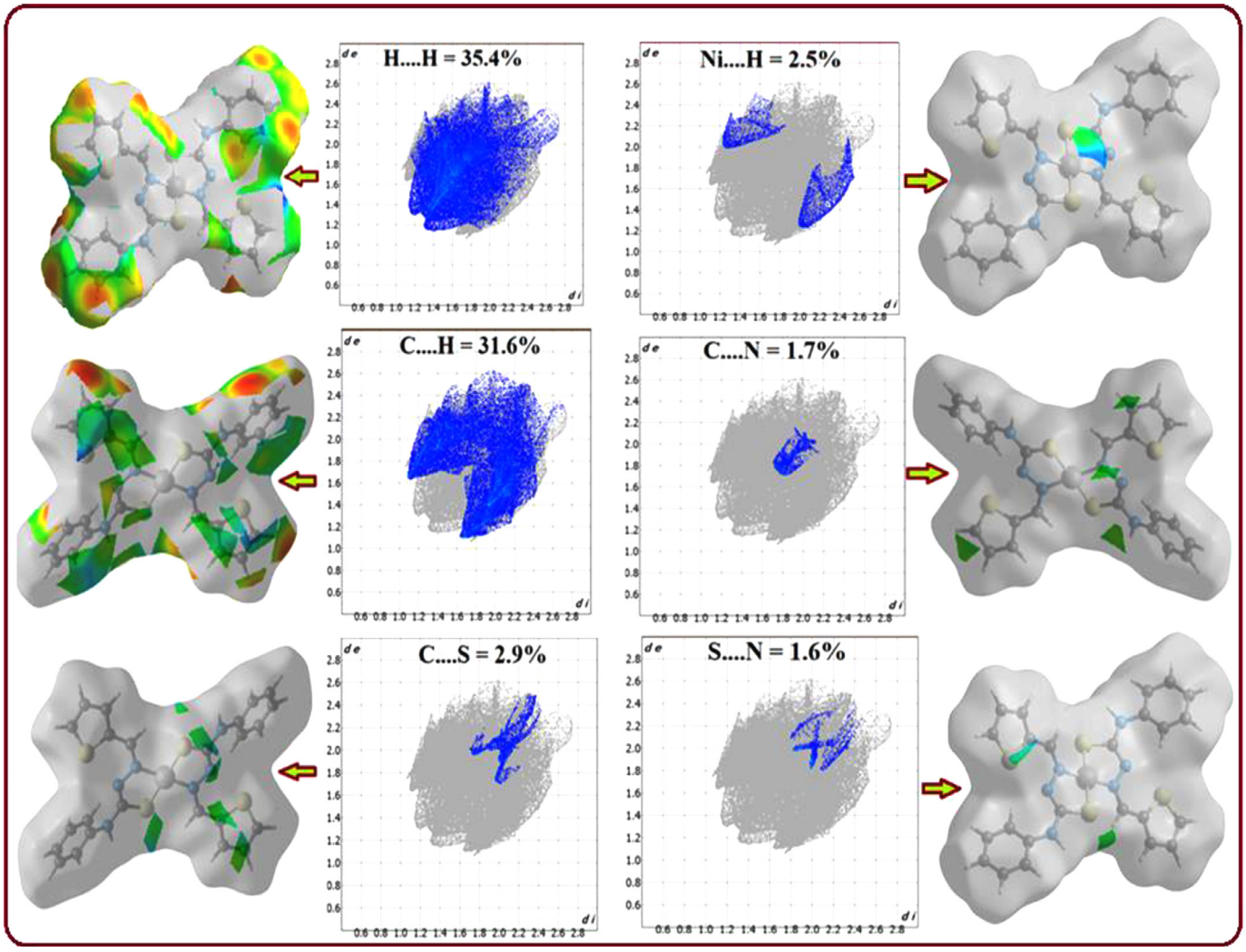

Fig. 5. Graphical view of Hirshfeld surface with 2D-fingerprint plots with characteristic features for Ni(II) complex [Ni(L_2)] (**1**): d_i and d_e are the distances from the surface to the nearest atoms interior and exterior to the surface respectively.

classical hydrogen bonds are represented by small red sports [55]. Shape index mapped over -1.0 to 1.0 au depending on the HS flatness or curvature, blue region shows hydrogen donor groups and a concave red region represents hydrogen acceptor groups. Fingerprint plots depicts that complementary region in plots can be visualized where one molecule behaves as a donor ($d_e > d_i$) while other behaves as an acceptor (de < di). These play an important role to illustrate the comparative contribution in terms of the percentage of various intermolecular interactions in the crystal lattice. It gives a quantitative summary of the nature and type of intermolecular contacts.

The two-dimensional (2D) fingerprint [56,57] plots generated corresponding to the H….H, C….H, C….S, Ni….H, C….N, and S….N for **(1)**. The H….H intermolecular contact is observed to be most and accounts for 35.4% of total HS for [Ni(L_2)] **(1)**. The proportion of other significant intermolecular interaction C….H/H….C, for **(1)** is found to be 31.6%. Further, C….S(2.9%), Ni….H(2.5%), C….N(1.7%), C….C(1.7%), S….S(0.2%) and S….N(1.6%) are the weak interaction of total HS for [Ni(L_2)] **(1)**. Figure S8 display the HS mapped with crystal void and deformation density of the ligand. Crystal Void is based on the sum of spherical atomic electron densities at the appropriate nuclear positions (procrystal electron density) [58]. The crystal-void calculation (results under 0.002 a.u. iso-value) shows the void volume of the **(1)** be of the order of 238.06 $Å^3$ and surface area in the order of 764.12 $Å^2$. The spatial distribution of the electrons involved in the chemical bonding can be studied through deformation density maps. The deformation density (results under 0.008 a.u. iso-value) was mapped over the range 0.008 to -0.008 au. The electron density deformation can be described as the subtraction of the electronic cloud of the molecule, minus the electronic cloud of the promolecule defined as the summation of the free atom spherical electron densities. The deformation is therefore positive between the bonds and negative at the nucleus.

Furthermore, energy framework computational analysis has been explored for the better understanding the nature of intermolecular interaction energies between the pair of molecules with a 3-D graphical representation of their magnitude [59]. Fig. 6 display the energy framework diagrams for **(1)** i.e. dispersion energy (E_{dis}), coulomb energy (E_{coul}), total energy (E_{tot}) and total (annotated) energy ($E_{tol.annot}$) which was calculated by generating a cluster of radii 3.8 Å around the molecule. The interaction energies for [Ni(L_2)] **(1)** was calculated with CE-B3LYP/6-31G(*d, p*)] model displayed in Table S1. It is suggested that the total energy consists of pair wise individual energy profiles such as E_{coul}, E_{dis}, E_{tot} and $E_{tol.annot}$. The tube size (250) connecting the centroids of the molecule represent the relative strength of the interaction, and tube color represents types of energy profiles of the intermolec-

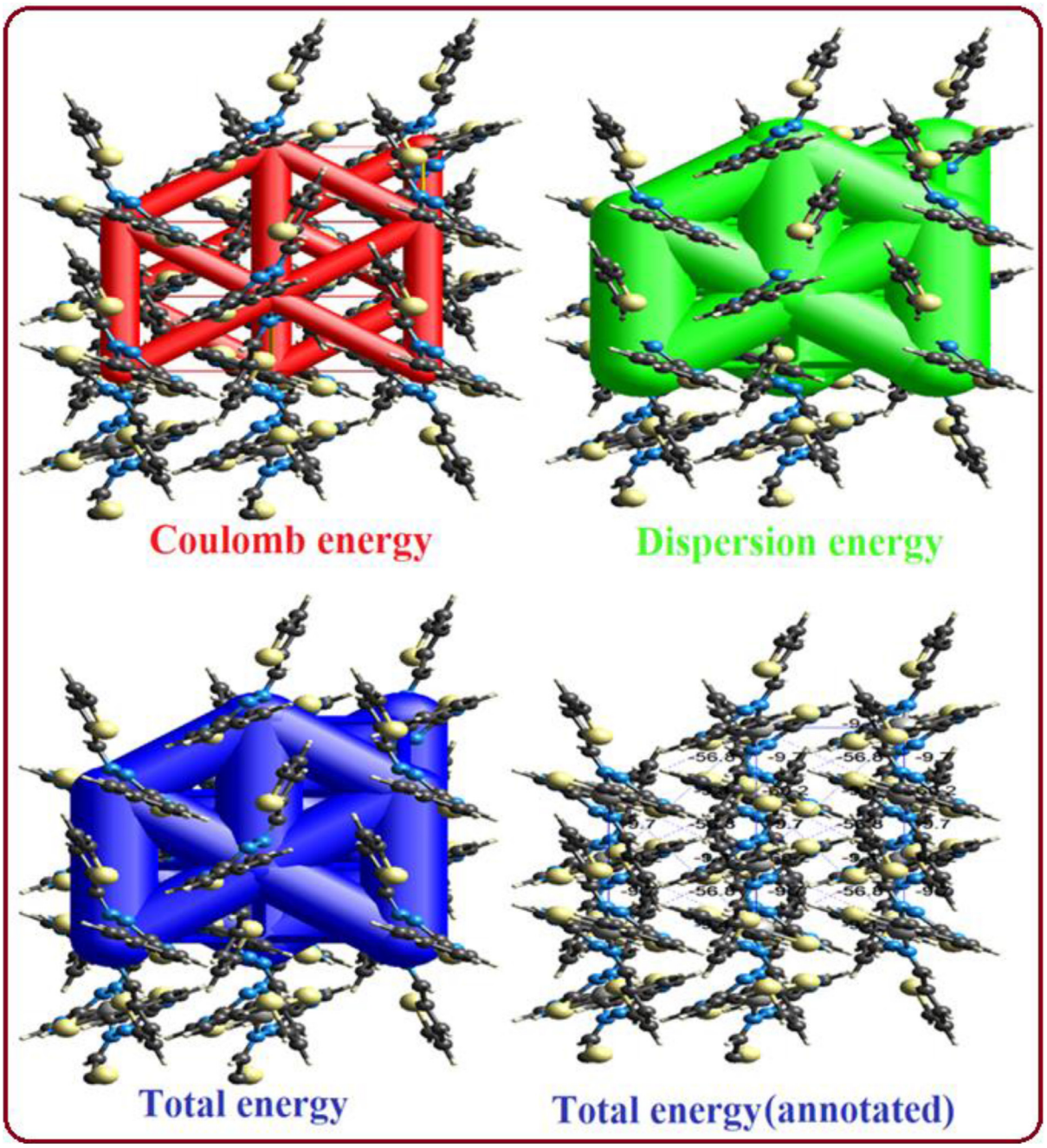

Fig. 6. Energy Framework diagrams for E_{coul}, E_{dis}, E_{tot} and $E_{tol.(annot)}$ for cluster of molecules in Ni(II) complex [$Ni(L_2)$] **(1).**

ular interaction energies. The lattice energy was calculated using the result obtained and was found to be -214.6 KJ/mol.

3.6. Frontier molecular orbital analysis

DFT has been proved to be best approach to investigate theoretically structure-property relationship for a compound as it shows excellent solution when both accuracy and computational time are taken in account [11]. FMO analysis provides the parameters for calculating the FMO energy gap which is used for describing the electronic structure of the compound [60,61]. 3D plots of frontier molecular orbital (FMOs) for Ni(II) complex [$Ni(L)_2$] **(1)** is given in Fig. 7 while FMOs diagrams for HL and its Cu(II) complex [$Cu(L)_2$] **(2)** are presented in Figure S9 and S10, respectively. The HOMO electron densities for **HL** is distributed mainly over sulfur and nitrogen atoms of thiosemicarbazone moiety and partially over the thiophene moiety, while the LUMO electron densities are distributed over the entire thiosemicarbazone moiety. The relatively higher HOMO energy of HL shows its electron donating ability. During HOMO-LUMO analysis, the relevant occupied and unoccupied MOs (HOMO/LUMO, HOMO-1/ LUMO+1 and HOMO-2/LUMO+2) are considered. The energy gaps are shown in Table 5. The energy gap was estimated at 1.39, 3.22 and 4.28 eV for **HL**, 0.15, 0.77 and 1.42 eV for complex [$Ni(L)_2$] (**1**) and 0.36, 1.17 and 1.29 eV for complex [$Cu(L)_2$] (**2**). It was noticed that the ligand **HL** has relatively higher energy gap than Ni(II) complex [$Ni(L)_2$] **(1)** and Cu(II) complex [$Cu(L)_2$] **(2)**.

The calculated molecular electrostatic potentials (MEPs) maps and electron density surfaces of all the synthesized compounds are given in Figure S11, which illustrates the three-dimensional charge

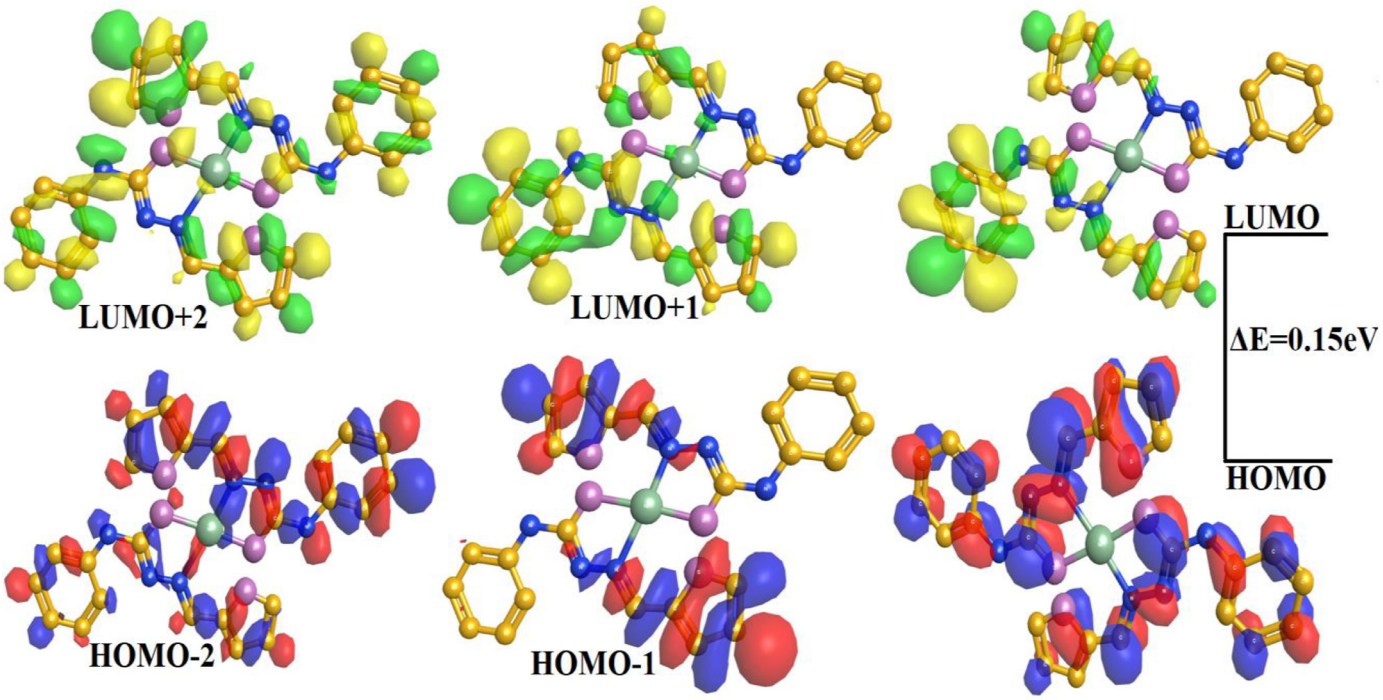

Fig. 7. Frontier molecular orbital diagram of nickel complex [Ni(L_2)] (**1**).

Table 4
The HOMO and LUMO energies and the energy gap (ΔE)[a] of Schiff base ligand **HL** and its Ni(II) complex [Ni(L_2)] **(1)** and Cu(II) complex [Cu(L_2)] **(2)**.

Compound	E_{LUMO}	E_{HOMO}	ΔE	$E_{LUMO\ (+1)}$	$E_{HOMO\ (-1)}$	ΔE	$E_{LUMO\ (+2)}$	$E_{HOMO\ (-2)}$	ΔE
HL	-0.03	-1.42	1.39	0.82	-2.39	3.22	1.03	-3.25	4.28
(1)	0.53	0.38	0.15	0.82	0.05	0.77	1.33	-0.09	1.42
(2)	0.71	0.36	0.36	1.40	0.23	1.17	1.62	-0.34	1.29

[a] Energy gap (ΔE) = E_{LUMO}-$E_{HOMO;}$ units in eV.

Table 5
Global reactivity descriptors [a] of the of Schiff base ligand **HL** and its Ni(II) complex [Ni(L_2)] **(1)** and Cu(II) complex [Cu(L_2)] **(2)**.

Molecular descriptors	Mathematical description	**HL**	**(1)**	**(2)**
Ionization potential (IP)	IP = - E_{HOMO}	1.42	-0.38	-0.36
electron affinity (EA)	EA = -E_{LUMO}	0.03	-0.53	-0.71
electro negativity (χ)	χ = (IP + EA)/2	0.73	-0.46	-0.53
chemical potential (μ)	η = (IP - EA)/2	0.70	0.07	0.36
global softness (σ)	μ = -(IP + EA)/2	-0.73	0.46	0.53
global hardness (η)	σ = 1/2η	0.72	6.85	1.40
Electrophilicity index (ω)	$\omega = \mu^2$ / 2 η	0.38	1.43	0.40

distributions within the molecules [62]. The MEPs is very useful descriptors to identify the electrophilic and nucleophilic reactive sites. Electrostatic potential map is drawn in the range -0.180 eV to 0.172 eV for Schiff base ligand (**HL**); -1.39 eV to –0.70 eV for Ni(II) complex [Ni(L_2)] **(1)**; while -1.72 eV to -1.06 eV for Cu(II) complex [Cu(L_2)] **(2)**. The red color represents the more electronegative sites and the positive sites are represented by blue color. Electrostatic potential map of the Schiff base ligand (**HL**) reflects the electron donating character (red color) for S of thiosemicarbazone and N of azomethine moiety that can be coordinated to metal ions, i.e active coordination centers. Global reactivity descriptors (units in eV), such as ionization potential (IP), electron affinity (EA), electro negativity (χ), chemical potential (μ), global hardness (η), global softness (σ) and global electrophilicity (ω), were calculated using the formulas based on Koopmans theorem [63]. The values of the global reactivity parameters are listed in Table 5. Overall, the electron donating and accepting abilities were described by ionization potential and electron affinity [64]. The Global reactivity parameters (GRPs) explicated that all the complexes showed greater electron affinity (EA) than the ionization potential (IP) (Table 5); hence, complexes have greater electron-accepting ability. The stability as well as reactivity of a chemical system was correlated to chemical potential and global hardness values [64]. The stability had a direct relation with global hardness, whereas it had an inverse relationship to its reactivity [65]. Thus, from the result obtain we can conclude that complex [Ni(L_2)] **(1)** is most stable having highest global hardness (-6.849 eV).

3.7. Molecular docking study

Molecular docking sheds light on designing drugs for the treatment of many diseases [66]. This technique allows us to study the binding of ligands to proteins having greater significance to screen virtual libraries of drug-like molecules [67]. For this consideration, we have purposefully docked all the synthesized compounds with the main protease (M^{Pro}) of protein (PDB ID: 7BZ5) of SARS-CoV-2 [44]. In Table 6, we have listed the obtained molecular docking results for **HL** and its metal complexes [Ni(L_2)] (**1**) and [Cu(L_2)] (**2**). These display the most important parameters including the binding affinity and different amino acid residues of M^{pro} that interact with the compounds. The molecular docking calculations of the ligand **HL** into the 7BZ5-main protease of SARS-CoV-2 virus revealed the binding energy of -7.2 kcal/mol, the binding energy of -9.7 kcal/mol for [Ni(L_2)] **(1)**, while [Cu(L_2)] **(2)** exhibited binding energy of -9.3 kcal/mol at the inhibition binding site of receptor protein. These binding affinities are reasonably well as compared to

Table 6
The molecular docking results for Schiff base ligand (**HL**) and its Ni(II) complex [$Ni(L_2)$] **(1)** and Cu(II) complex [$Cu(L_2)$] **(2)** with SARS-COv-2 M^{Pro} (PDB ID: 7BZ5) and HIV-1 virus (PDB ID: 6MQA) including the binding affinity and different amino acid residues of proteins that interact with the compounds.

Molecule		Binding affinity (kcal/mol)	Interacting residues		
			H-bond	Electrostatic	Hydrophobic
HL	7BZ5	-7.2	TYR-453(3.4 Å) SER-93(3.4 Å) TYR-97(3.3 Å) ASN-92(2.3 Å) GLU-98(3.1 Å) TYR-52(3.3 Å)	GLU-98(3.7 Å)	TYR-58(5.0 Å) TYR-94(5.3 Å) LEU-455(5.4 Å)
	6MQA	-6.8	ASN-53(2.35 Å) ASN-57(2.97 Å) LYS-70(4.12 Å)	ASN-57(2.75 Å)	LYS-70(4.22 Å) LEU-56(3.58 Å) LEU-69(5.07 Å)
(1)	7BZ5	-9.7	GLU-166(5.3 Å) GLU-150(12.5 Å) SER-9(6.0 Å) GLU-102(4.7 Å)	ARG-143(3.4 Å) ALA-43(8.0 Å)	LEU-45(8.7 Å) VAL-171(12.9 Å)
	6MQA	-8.5	GLN-179(5.5 Å) LEU-211(6.8 Å)	ASN-153(6.7 Å) GLY-208(4.5 Å)	GLN-179(6.4 Å) GLN-179(6.0 Å)
(2)	7BZ5	-9.3	SER-134(4.9 Å) PHE-119(1.7 Å)	LEU-202(1.3 Å) THR-162(2.9 Å)	THR-165(3.2 Å) SER-169(35.6 Å) ARG-143(2.5 Å)
	6MQA	-8.2	ALA-105(3.9 Å) MET-66(11.3 Å) LYS-70(3.9 Å)	ILE-134(8.1 Å) TRP-23(19.0 Å)	ALA-105(8.4 Å) THR-48(3.4 Å) MET-55(5.0 Å)

recently docked results of anti-SARS-CoV-2 drugs like chloroquine, hydroxychloroquine, and remdesivir with M^{pro} protein. It is evident from the Figure S12 that **HL** was surrounded by residues Tyr-453, Ser-93, Tyr-97, Asn-92, Glu-98, Tyr-52, Glu-98, Tyr-58, Tyr-94 and Leu-455 of protein (PDB ID: 7BZ5); [$Ni(L)_2$] **(1)** was surrounded by protein residues Glu-166, Glu-150, Ser-9, Glu-102, Arg-143, Ala-43, Leu-45 and Val-171 (Fig. 8); while [$Cu(L)_2$] **(2)** was surrounded by protein residues Ser-134, Phe-119, Leu-202, Thr-162, Thr-165, Ser-169 and Arg-143 (Figure S13). Leu-455 forms alkyl interaction with phenyl ring of ligand **HL**. Phe-119 amino acid form π-sigma interaction with phenyl ring of **(2).** The result obtained shows that the binding energy of metal complexes at the binding site of receptor protein is greater compared to free ligand.

Molecular docking result for Schiff base ligand (**HL)** and its metal complexes against HIV-1 CA virus (PDB ID: 6MQA)[45] are tabulated in Table 6. Figure S14 shows that **HL** wasvsurrounded by Asn-53, Asn-57, Lys-70, Asn-57, Lys-70, Leu-56 and Leu-69 residues of HIV-1 CA protein (PDB ID: 6MQA); [$Ni(L)_2$] **(1)** was surrounded by residues Gln-179, Leu-211, Asn-153, Gly-208, Gln-179, Gln-179 (Fig. 9); while [$Cu(L)_2$] **(2)** was surrounded by Ala-105, Met-66, Lys-70, Ile-134, Trp-23, Ala-105, Thr-48 and Met-55 (Figure S15). The results shows the binding affinity (-8.5 Kcal/mol) of Ni(II) complex [$Ni(L)_2$] (**1**) at the binding site of receptor protein of HIV-1 is greatest. Molecular docking result also reveals that all the synthesized compounds shows higher binding energy against the main protease (M^{Pro}) of protein (PDB ID: 7BZ5) of SARS-CoV-2 than HIV-1 virus (PDB ID: 6MQA). Moreover, Ni(II) complex [$Ni(L)_2$] **(1)** shows better result than **HL** and Cu(II) complex [$Cu(L)_2$] **(2)** when docked against the proteins SARS-CoV-2 than HIV-1 virus (PDB ID: 7BZ5 and 6MQA). The binding affinities of the studied new Schiff base ligand and their metal complexes were found to be better than other metal complexes reported using molecular docking techniques [68,69].

Figure S16 represents the total density surfaces [60] representation for docked Ni(II) complex [$Ni(L)_2$] **(1)** inside the M^{Pro} protein (PDB ID: 7BZ5); (a) with hydrogen bond donor and acceptor meshes represented by pink and red colors, respectively; (b) surface representation of hydrophobic pocket represented with blue and red colors. Figure S17 represents the total density surfaces representation for docked Cu(II) complex [$Cu(L)_2$] **(2)** inside the SARS-CoV-2 M^{Pro} protein (PDB ID: 7BZ5); (a) with hydrogen bond donor and acceptor meshes represented by green and red colors, respectively; (b) surface representation of hydrophobic pocket represented with deep blue and violet colors.. Figure S18 represents the total density surfaces representation for docked Ni(II) complex [$Ni(L)_2$] (**1**) inside the HIV- virus (PDB ID: 6MQA). (a) with hydrogen bond donor and acceptor meshes represented by orange and blue colors, respectively; (b) surface representation of hydrophobic pocket represented with blue and red colors. Figure S19 represents the total density surfaces representation for docked Cu(II) complex [$Cu(L)_2$] **(2)** inside the HIV- virus (PDB ID: 6MQA). (a) with hydrogen bond donor and acceptor meshes represented by light green and blue colors, respectively; (b) surface representation of hydrophobic pocket represented with purple and red colors. A structural activity relationship has been established [59] between the experimental bond lengths data of Ni(II) complex [$Ni(L)_2$](**1**) obtained from X-ray crystallography and bond lengths data obtained from molecular docking results with SARS-CoV-2 and HIV virus (Table S2). The structure-activity comparison shows good correlation between results obtained from experimental and theoretical methods.

3.8. Swiss-ADME analysis

The potential theoretical biological activities of all the synthesized Schiff base ligand **HL** and its metal complexes [$Ni(L)_2$] **(1)** and [$Cu(L)_2$] **(2)** were virtually designed *in silico* evaluation. To be effective as a drug for the patients, a potent molecule must reach its target in the body in sufficient concentration, and stay there in a bioactive form long enough for the expected biologic events to occur. Drug development involves assessment of absorption, distribution, metabolism, and excretion (ADME) increasingly earlier in the drug discovery process. Comparative results are summarized in the Table S3. The HL attained all the drug likeness properties. While both the complexes [$Ni(L)_2$] **(1)** and [$Cu(L)_2$] **(2)** failed to attain only two Lipinski's rule [70] which is their molecular weight and Log P value. However, they are suitable for pharmacokinetics response. These complexes are predicted not orally bioavailable, because too flexible and too polar structures. Figure S20 shows Swiss target prediction representative available on Swiss-

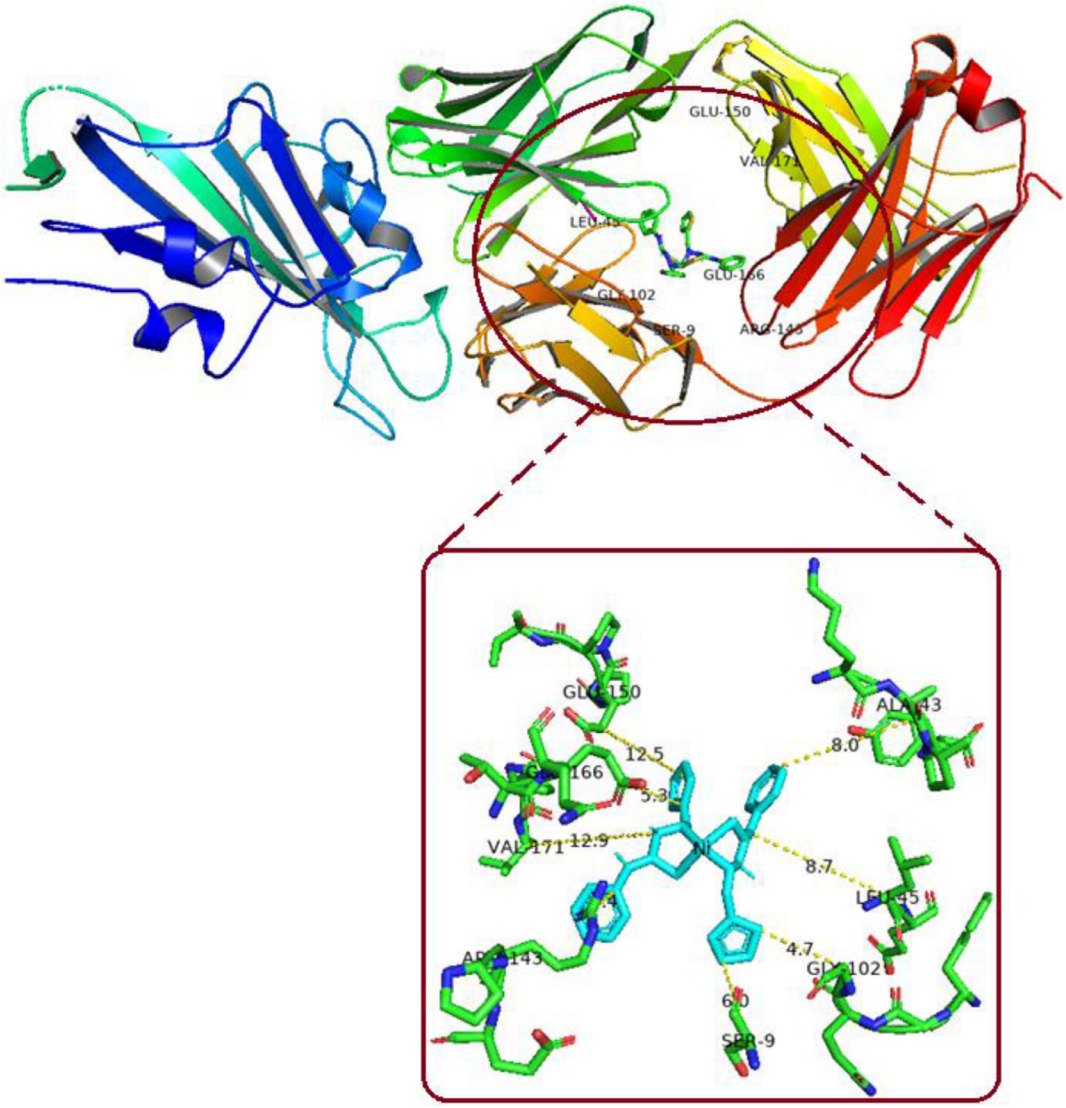

Fig. 8. The docked Ni(II) complex [$Ni(L_2)$] **(1)** inside the SARS-CoV-2 M^{pro} (PDB ID: 7BZ5) with its focused view for interacting residues around the docked complex.

ADME [71] submission page for all the synthesized compounds. The Schiff base ligand and its complexes are substrate or inhibitor of isoenzymes governing important pharmacokinetic behaviors and pharmacokinetics related drug-drug interactions. The Swiss-ADME analysis results of ligand **HL** and its metal complexes [$Ni(L)_2$] **(1)** and [$Cu(L)_2$] **(2)** are to be found comparatively higher than that of chloroquine (CQ) and Hydroxychloroquine (HCQ) as anti-SARS-CoV-2 drugs [69].

3.9. Conclusions

In conclusion, we successfully, designed, synthesized and explored anti-virus potential of two new coordination complexes, a Ni(II) complex [$Ni(L)_2$] (**1**) and a Cu(II) complex [$Cu(L)_2$] (**2**) of (E)-N-phenyl-2-(thiophen-2-ylmethylene) hydrazine-1-carbothioamide(**HL**). Single-crystal X-ray diffraction reveals that Ni(II) center of the complex [$Ni(L)_2$] (**1**) exhibits a distorted square planar geometry coordinated to two symmetrically equivalent thiosemicarbazone Schiff base **HL** anions which completely balances Ni^{+2} cation. Powdered XRD patterns of the **HL** and its copper (II) complex [$Cu(L)_2$] (**2**), shows several diffraction peaks clearly prove their formation. The XRD patterns of the Schiff bases were observed at 2 θ = 22.36º for **HL,** which is characteristic peak for a Schiff base imine. The Hirshfeld surface (HS) for nickel(II) complex [$Ni(L)_2$] **(1)** is analyzed to evaluate the intermolecular interaction in the crystal system. The lattice energy was calculated using the result obtained and was found to be -214.6 KJ/mol. We have successfully docked all the synthesized compounds with the main protease (M^{Pro}) of protein (PDB ID: 7BZ5) of SARS-CoV-2 and HIV-1 virus (PDB ID: 6MQA). Molecular docking result reveals that Schiff base ligand **HL** (-7.2 Kcal/mol), Ni(II) complex [$Ni(L)_2$] **(1)** (-9.7 Kcal/mol) and Cu(II) complex [$Cu(L)_2$] **(2)** (-9.3 Kcal/mol) shows higher binding energy against the main protease (M^{Pro}) of protein (PDB ID: 7BZ5) of SARS-CoV-2 than HIV-1 virus (PDB ID: 6MQA). Moreover, Ni(II) complex [$Ni(L)_2$] (**1**) shows better result than **HL** and Cu(II) complex [$Cu(L)_2$] **(2)** when docked against the SARS-CoV-2 than HIV-1 virus proteins (PDB ID: 7BZ5 and 6MQA). These synthesized compounds also exhibited pharmacokinetics response.

Supplementary material Deposition Number: CCDC-2152930 for [$Ni(L)_2$ **(1)** contains the supplementary crystallographic data for this paper. This data can be obtained free of charge at www.ccdc.cam.ac.uk/ conts/retrievel.html or www.ccdc.cam.ac.uk/structures or from the Cambridge Crystallographic Data Center, 12 Union Road, Cambridge CB2 1EZ, UK; fax: +44 1223/ 336 033. Email: deposit@ccdc.ac.uk.

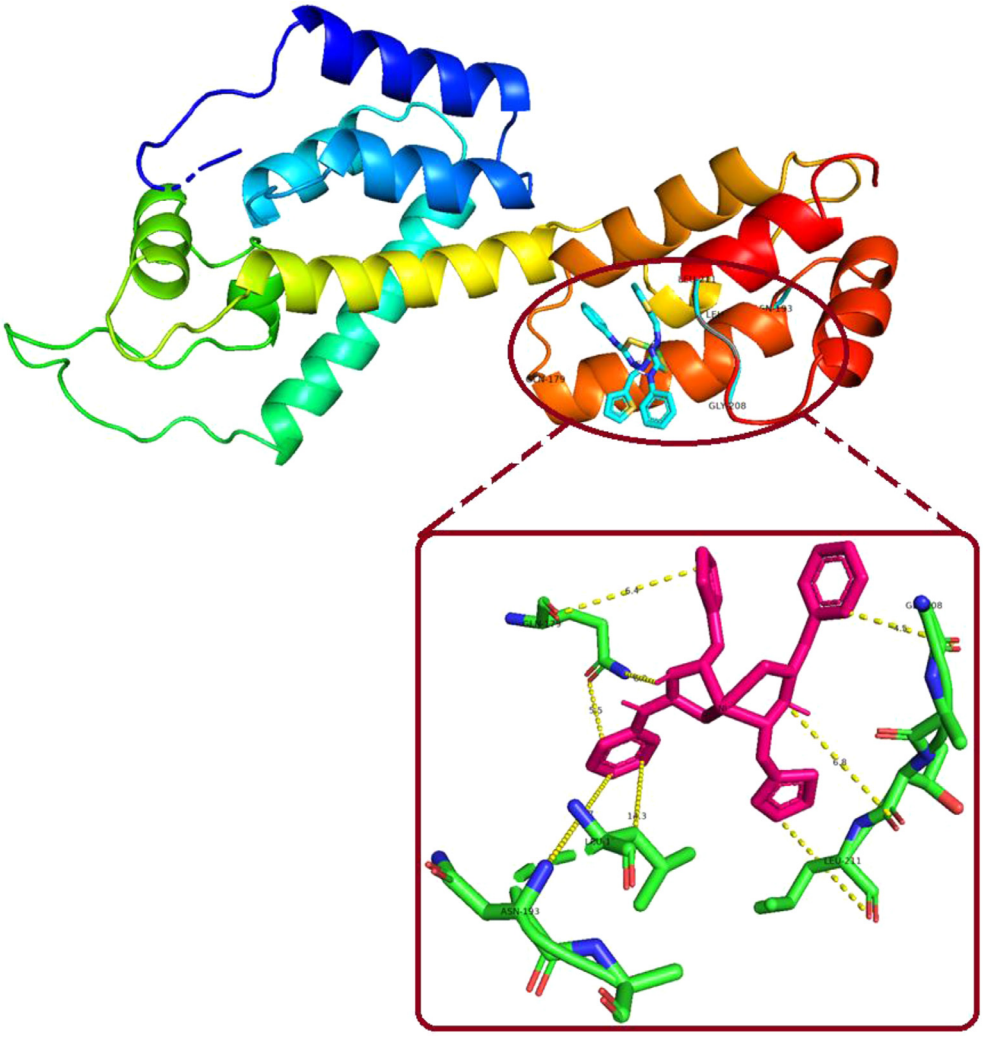

Fig. 9. The docked nickel(II) complex [Ni(L_2)] (**1**) inside the HIV-1 virus (PDB ID: 6MQA) with its focused view for interacting residues around the docked complex.

Declaration of Competing Interest

The authors declare that they have no known competing financial interests or personal relationships that could have appeared to influence the work reported in this paper.

CRediT authorship contribution statement

Aprajita: Formal analysis, Investigation, Software, Writing – original draft, Resources. **Mukesh Choudhary:** Supervision, Conceptualization, Data curation, Visualization, Methodology.

Acknowledgement

We wish thanks to SAIF, IIT Madras for Single crystal X-ray analysis of Ni(II) complex [Ni(L_2)] (**1**). Also thanks to SAIF, IIT Madras for spectral analysis (NMR and IR analysis). The authors are thankful to the Head, Chemistry Department, National Institute of Technology Patna for providing computational resources and spectral analysis. One of the authors (Aprajita) thanks to CSIR, New Delhi, India for awarding JRF fellowship (File no. 09/1278(0003)/2020-EMR-I).

Supplementary materials

Supplementary material associated with this article can be found, in the online version, at doi:10.1016/j.molstruc.2022.133114.

References

[1] O.K. Nehar, R. Mahboub, S. Louhibi, T. Roisnel, M. Aissaoui, J. Mol. Struct. 1204 (2010) 127566.
[2] M.S. More, P.G. Joshi, Y.K. Mishra, P.K. Khanna, Mater Today Chem 14 (2019) 100195.
[3] R. Basri, M. Khalid, Z. Shafiq, M.S. Tahir, M.U. Khan, M.N. Tahir, M.M. Naseer, A.A.C. Braga, ACS Omega. 5 (2020) 30176–30188.
[4] T.S. Lobana, R. Sharma, G. Bawa, S. Khanna, Coord. Chem. Rev. 253 (2009) 977–1055.
[5] S. Savir, J.W.K. Liew, I. Vythilingam, Y.A.L. Lim, C.H. Tan, K.S. Sim, V.S. Lee, M.J. Maah, K.W. Tan, J. Mol. Struct. 1242 (2021) 130815.
[6] J.M. Jacob, M.R.P. Kurup, K. Nisha, G. Serdaroglu, S. Kaya, Polyhedron 189 (2020) 114736.
[7] P.F. Rapheal, E. Manoj, M.R.P. Kurup, H. Fun, J. Mol. Struct. 1237 (2021) 130362.
[8] M. Sobiesiak, M. Cieslak, K. Krolewska, J. Kazmierczak-Baranska, B. Pasternakc, E. Budziszd, New J. Chem. 40 (2016) 9761–9767.
[9] K. Ohui, E. Afanasenko, F. Bacher, R.L.X. Ting, A. Zafar, N. Blanco-Cabra, E. Torrents, O. Domotor, N.V. May, D. Darvasiova, E.A. Enyedy, A. Popovic-Bijelic, J. Reynisson, P. Rapta, M.V. Babak, G. Pastorin, V.B. Arion, J. Med. Chem. 62 (2019) 512–530.
[10] S. Kathiresan, S. Mugesh, J. Annaraj, New J. Chem 41 (2017) 1267–1283.

[11] R. Fouad, I.A. Shaaban, T.E. Ali, M.A. Assiri, S.S. Shenouda, RSC Adv. 11 (2021) 377726.
[12] L. Dkhar, V. Banothu, K.M. Poluri, W. Kaminski, M.R. Kollipara, J. Organomet. Chem. 918 (2020) 121298.
[13] E. Türkkan, U. Sayin, N. Erbilen, S. Pehlivanoglu, G. Erdogan, H.U. Tasdemir, A.O. Saf, L. Guler, E.G. Akgemci, J. Organomet. Chem. 831 (2017) 23–35.
[14] R.A. Bedier, T.A. Yousef, G.M. Abu El-Reash, O.A. El-Gammal, J. Mol. Struct. 1139 (2017) 436–446.
[15] C.C. Gatto, P.M. Miguel, C.M. Almeida, P.H.O. Santiago, C.R.K. Paier, C. Pessoa, Transit Met Chem 42 (2017) 503–508.
[16] S. Kumar, S. Muhammad, S.S. Alarfaji, S. Yoon, M. Kim, K. Youm, M. Khalid, A.R. Chaudhary, J. Koh, Optik. 246 (2021) 167748.
[17] P. Debnath, S. Bhaumik, D. Sen, S. Debnath, Chemistry Select 6 (20) (2021) 4991–5013.
[18] S. Kumar, M. Choudhary, New J. Chem. (2022), doi:10.1039/D2NJ00703G.
[19] A. Andreou, S. Trantza, D. Filippou, S. Tsiodras, Vivo (Brooklyn) 34 (2020) 1567–1588.
[20] G.M. Sheldrick, Acta Crystallogr 71 (2015) 3–8 C.
[21] D. Fu, J. Gao, W. He, X. Huang, Y. Liu, Y. Ai, Angew. Chem. Int. Ed. 59 (2020) 17477.
[22] L.J. Farrugia, J. Appl. Crystallogr. 45 (2012) 849–854.
[23] C.F. Macrae, P.R. Edgington, P. McCabe, E. Pidcock, G.P. Shields, R. Taylor, M. Towler, J. van de Streek, J. Appl. Crystallogr. 39 (2006) 453–457.
[24] K. Brandenburg, Diamond version 3.2k, Crystal Impact GbR, Bonn, Germany, 2014 http://www.crystalimpact.com/diamond.
[25] S. Kumar, M.Y. Wani, C.T. Arranja, R.A.E. Castro, J.A. Paixao, A.J.F.N. Sobral, Spectrochim. Acta Part A 188 (2018) 183–188.
[26] S. Ide, N. Anc, S.G. Oztas, M. Tuzun, J. Mol. Struct. 562 (2001) 1–9.
[27] M.S. Nair, D. Arish, R.S. Joseyphus, J. Saudi Chem. Soc 16 (2012) 83–88.
[28] M.J. Turner, J.J. Mckinnon, S.K. Wolff, D.J. Grimwood, P.R. Spackman, D. Jayatilaka, M.A. Spackman, Crystal Explorer, 17, The University of Western Australia, 2017 https://hirshfeldsurface.net.
[29] K. Kumara, A.D. Kumar, K.A Kumar, N.K. Lokanath, Chem. Data Collect. 13 (2018) 40.
[30] H.M. Mahesha, C.S. Krishnegowda, P.J. Karthik, P. Kudigana, Mallu, N.K. Lokanath, Polyhedron 185 (2020) 114571.
[31] C.F. Mackenzie, P.R. Spackman, D. Jayatilaka, M.A. Spackman, IUCrJ 4 (2017) 575–587.
[32] S.M. Kumar, B.N. Lakshminarayana, S. Nagaraju, S. Ananda, B.C. Manjunath, N.K. Lokanath, K. Byrappa, J. Mol. Struct. 1173 (2018) 300–306.
[33] S.L. Tan, M.M. Jotani, E.R. Tiekink, Acta Cryst. E. 75 (2019) 308–318.
[34] M.J. Frisch, G.W. Trucks, H.B. Schlegel, G.E. Scuseria, M.A. Robb, J.R. Cheeseman, G. Scalmani, V. Barone, B. Mennucci, G.A. Petersson, Gaussian 16 Rev. A.03, Wallingford, CT, 2016.
[35] H. Lambert, N. Mohan, T.C. Lee, Phys. Chem. Chem. Phys. 21 (2019) 14521–14529.
[36] J.D. Chai, M.H. Gordon, Phys. Chem. Chem. Phys. 10 (2008) 6615–6620.
[37] M.M. Matin, M. Uzzaman, S.A. Chowdhury, M.M.H. Bhuiyan, , J. Biomol. Struct. Dyn. (2020), doi:10.1080/07391102.2020.1850358.
[38] C. Shivanika, S.D. Kumar, V. Ragunathan, P. Tiwari, A. Sunitha, J. Biomol. Struct. Dyn. (2020), doi:10.1080/07391102.2020.1815584.
[39] A. Daina, Vincent Zoete, Chem. Med. Chem. 11 (2016) 1117–1121.
[40] A. Daina, O. Michielin, V. Zoete, Sci. Rep 7 (2017) 42717.
[41] Y. Wu, F. Wang, C. Shen, W. Peng, D. Li, C. Zhao, Z. Li, S. Li, Y. Bi, Y. Yang, Y. Gong, H. Xiao, Z. Fan, S. Tan, G. Wu, W. Tan, X. Lu, C. Fan, Q. Wang, Y. Liu, C. Zhang, J. Qi, G.F. Gao, F. Gao, L. Liu, Science 368 (2020) 1274–1278.
[42] S.S. Smaga, C. Xu, B.J. Summers, K.M. Digianantonio, J.R. Perilla, Y. Xiong, Structure 27 (2019) 1273.
[43] H. Park, J. Lee, S. Lee, Proteins 65 (2006) 549–554.
[44] D. Seeliger, B.L. de Groot, J. Comput. Aided Mol. 24 (2010) 417–422.
[45] D.S. Biovia, Discovery Studio Visualizer, v17.2.0.16349, Dassault Systems, San Diego, 2016.
[46] S. Savir, Z.J. Wei, J.W.K. Liew, I. Vythilingam, Y.A.L. Lim, H.M. Saad, K.S. Sim, K.W. Tan, J. Mol. Struct. 1211 (2020) 128090.
[47] A. Akbari, H. Ghateazadeh, R. Takjoo, B. Sadeghi-Nejad, M. Mehrvar, J.T. Mague, J. Mol. Struct. 1181 (2019) 287e294.
[48] D. Aggoun, M. Fernandez-Garcia, D. Lopez, B. Bouzerafa, Y. Ouennoughi, F. Setifi, A. Ourari, Polyhedron 187 (2020) 114640.
[49] M. Fallah-Mehrjardi, H. Kargar, R. Behjatmanesh-Ardakani, M. Ashfaq, K. Shahzad Munawar, M.N. Tahir, J. Mol. Struct. 1251 (2022) 132037.
[50] S. Guvelia, I. Kılıç-Cıklab, B. Ulkusevena, M. Yavuzc, T. Bal-Demircia, J. Mol. Struct 1173 (2018) 366–374.
[51] M. Biswasa, E.C. Sanudo, J. Cirera, D. Ray, New J. Chem. 44 (2020) 4812–4821.
[52] M.S. Nair, D. Arish, R.S. Joseyphus, J. Saudi Chem. Soc 16 (2012) 83–88.
[53] L. Latheef, M.R.P. Kurup, E. Suresh, Chem. Data Coll. 35 (2021) 100758.
[54] P.F. Rapheal, E. Manoj, M.R.P. Kurup, H. Fun, J. Mol. Struct. 1237 (2021) 130362.
[55] M.C. Vineetha, F. Joy, K.P. Murali, T.P. Vinod, S.K. Venkataraman, A.K. Agarwal, Y. Nair, M.R.P. Kurup, Appl. Organomet. Chem. 35 (9) (2021) e6334.
[56] K.K.M. Hashim, E. Manoj, M.R.P. Kurup, J. Mol. Struct. 1246 (2021) 131125.
[57] Y. Xie, Y. Ai, Y. Zeng, W. He, X. Huang, D. Fu, J. Gao, X. Chen, Y. Tang, J. Am. Chem. Soc. 142 (2020) 12486.
[58] S. Kumar, M. Chodhary, J. Biomol. Struct. Dyn. (2021), doi:10.1080/07391102.2021.2006089.
[59] S. Kumar, M. Choudhary, New J. Chem. 46 (2022) 4911–4926.
[60] S. Kumara, S. Muhammad, J. Koha, M. Khalid, K. Ayubd, Optik. 192 (2019) 162952.
[61] R.N. Patel, S.K. Patel, D. Kumhar, N. Patel, A.K. Patel, R.N. Jadeja, N. Patel, B.J. Butcher, M. Carijo, S. Herrero, Polyhedron 188 (2020) 114687.
[62] J.J. Murray, P. Politzer, WIRES, Comput. Mol. Sci 1 (2011) 153–322.
[63] T. Koopmans, Physica 1 (1934) 104–113.
[64] S. Murugavel, V.V. Velan, D. Kannan, M. Bakthadoss, J. Mol. Struct. 1108 (2016) 150–167.
[65] P.F. Rapheal, E. Manoj, M.R.P. Kurup, H. Fun, J. Mol. Struct. 1237 (2021) 130362.
[66] S. Boopathi, A.B. Poma, P. Kolandaivel, J. Biomol. Struct. Dyn. (2020) 1–10.
[67] S. Kumar, G. Kumar, I.C. Shukla, SN Appl. Sci. 2 (2020) 1241.
[68] G. Abbas, A. Irfan, I. Ahmed, F. Zeidaneen, S. Muthu, O. Fuhr, R. Thomas, J. Mol. Struct. 1253 (2022) 132242.
[69] A. Ali, N. Sepay, M. Afzal, N. Sepay, A. Alarifi, M. Shahid, M. Ahmad, Bioorg. Chem. 110 (2021) 104772.
[70] B. Mohan, M. Choudhary, S. Muhammad, N. Das, K. Singh, A. Jana, S. Bharti, H. Algarni, A.G. Al-Sehemi, S. Kumar, J. Coord. Chem. 73 (8) (2020) 1256–1279.
[71] B. Mohan, M. Choudhary, G. Kumar, S. Muhammad, N. Das, K. Singh, A.G. Al-Sehemi, S. Kumar, Synth. Commun. 50 (14) (2020) 2199–2225.